PNAS RESEARCH ARTICLE | BIOPHYSICS AND COMPUTATIONAL BIOLOGY
MICROBIOLOGY

Reduced surface accumulation of swimming bacteria in viscoelastic polymer fluids

Ding Cao[a,1], Mariia Dvoriashyna[b,1,2], Song Liu[a,1,3], Eric Lauga[b,4], and Yilin Wu[a,4]

Edited by Herbert Levine, Northeastern University, Boston, MA; received July 14, 2022; accepted October 2, 2022

Surface-associated bacterial communities flourish in nature and in the body of animal hosts with abundant macromolecular polymers. It is unclear how the endowed viscoelasticity of polymeric fluids influences bacterial motile behavior in such environments. Here, we combined experiment and theory to study near-surface swimming of flagellated bacteria in viscoelastic polymer fluids. In contrast to the swimming behavior in Newtonian fluids, we discovered that cells swim in less curved trajectories and display reduced near-surface accumulation. Using a theoretical analysis of the non-Newtonian hydrodynamic forces, we demonstrated the existence of a generic lift force acting on a rotating filament near a rigid surface, which arises from the elastic tension generated along curved flow streamlines. This viscoelastic lift force weakens the hydrodynamic interaction between flagellated swimmers and solid surfaces and contributes to a decrease in surface accumulation. Our findings reveal previously unrecognized facets of bacterial transport and surface exploration in polymer-rich environments that are pertinent to diverse microbial processes and may inform the design of artificial microswimmers capable of navigating through complex geometries.

flagellar motility | hydrodynamics of microorganisms | bacterial transport | viscoelasticity | elastic tension

Significance

Many bacteria live in natural and clinical environments with abundant macromolecular polymers. Flagellar motility in these polymeric fluids is essential to diverse microbial processes, such as bacterial dispersal and colonization. While geometrical confinement or surfaces are prevalent in the living environment of bacteria, it is unclear how flagellated bacteria interact with surfaces in polymeric fluids. Here, we found that non-Newtonian hydrodynamic interaction between flagellated bacteria and a solid surface gives rise to a viscoelastic lift force acting on the cells; this lift force leads to several unusual behavioral patterns in contrast to swimming in Newtonian viscous fluids. Our findings will help to understand the transport of bacteria and artificial helical microswimmers in macromolecular environments with ecological and clinical relevance.

Many bacteria live in natural and clinical environments with abundant macromolecular polymers, such as biofilm matrices (1), intestinal outer mucus layer (2), and extracellular matrices (3). Flagellar motility in these polymeric fluids is essential to diverse microbial processes (4), such as biofilm formation (5), bacterial transport (6), and pathogen invasion (7). Polymeric fluids commonly display viscoelasticity and non-Newtonian rheological behavior (8), and how these fluid properties affect bacterial swimming behavior has been a long-standing question (9–13). More recent work primarily studied bacterial swimming behavior in bulk fluids, with a focus on the effects of viscoelasticity and shear-thinning viscosity on the intriguing phenomenon of speed enhancement (14–17). However, it is unclear how swimming bacteria interact with boundaries in polymeric fluids, despite the fact that geometrical confinement or solid surfaces are prevalent in the living environment of bacteria (4). This topic has only received attention from theoretical perspectives with simplified cell-surface hydrodynamic interactions (18) or with simplified swimmer configurations, such as a spherical squirmer without rotating flagellum (19–21).

Here, we combined experiment and theory to study near-surface swimming of flagellated bacteria in viscoelastic polymeric fluids. In contrast to the well-known circular swimming behavior in Newtonian fluids (22–27), we discovered that cells swim in less curved trajectories near solid surfaces, with the mean radius of curvature increasing with polymer concentrations; meanwhile, cell density profiles showed that the extent of near-surface accumulation, another phenomenon familiar in Newtonian fluids (28–32), also decreased with polymer concentration. To explain these findings, we developed a non-Newtonian hydrodynamic model of a swimming cell next to a plane wall, focusing on the role of the rotating flagellar filaments. We demonstrated the existence of a generic lift force acting on a rotating filament near a rigid surface (i.e., a net force away from the surface). This lift arises from the elastic tension generated along curved streamlines by polymer stresses (33). This viscoelastic lift force weakens the hydrodynamic interaction between flagellated swimmers and the nearby surface, thereby reducing the extent of cell accumulation near surfaces and the magnitude of curvature of cell trajectories. The viscoelastic lift we uncovered, as well as the resulting motion pattern of microswimmers, may enhance the efficiency of bacterial transport (34) and surface exploration (35). The mechanism could also be exploited to design artificial microswimmers (36) capable of navigating through complex geometries (37) with adaptive locomotion patterns.

The authors declare no competing interest.

This article is a PNAS Direct Submission.

[1]D.C., M.D., and S.L. contributed equally to this work.

[2]Current affiliation: Mathematical Institute, University of Oxford, Oxford OX2 6GG United Kingdom

[3]Current affiliation: Department of Physics, Southern University of Science and Technology, Shenzhen, 518055, People's Republic of China

[4]To whom correspondence may be addressed. Email: e.lauga@damtp.cam.ac.uk or ylwu@cuhk.edu.hk.

This article contains supporting information online at http://www.pnas.org/lookup/suppl/doi:10.1073/pnas.2212078119/-/DCSupplemental.

Published November 2, 2022.

Results

Viscoelasticity of Polymeric Fluids Reduces the Absolute Curvature of Bacterial Trajectories Near Surfaces. To investigate the near-surface motion pattern of bacteria swimming in polymeric fluids, we chose to study the model flagellated bacterium *Escherichia coli* (*E. coli*). Wild-type *E. coli* performs run-and-tumble motion regulated by the chemotactic signaling pathway (38). Although tumbling is suppressed by cell–surface hydrodynamic interactions (30), we wanted to completely exclude this effect and thus used a smooth-swimming (i.e., nontumbling) mutant of *E. coli* (*Materials and Methods*). Viscoelastic polymeric fluids consisting of salmon testes DNA (hereafter referred to as DNA; *Materials and Methods*) were primarily used in this study, because they display strong shear-thinning viscosity and thus support normal bacterial swimming speed at relatively high concentrations (39). By tracking the motion of *E. coli* near glass surfaces immersed in the viscoelastic fluids with 3D defocused fluorescence microscopy (40) (Fig. 1*A*), we extracted the trajectories of cells within 5 μm from the surface (*Materials and Methods*). In Newtonian fluids, flagellated bacteria swim in circles near a solid surface due to a surface-induced hydrodynamic torque acting on the swimming cell (23, 24), and the magnitude of curvature appeared to slightly increase with viscosity (*SI Appendix*, Fig. S1) presumably due to torque variation resulting from the load-dependent flagellar remodeling (41). In stark contrast, in viscoelastic DNA solutions, we found that cells swam in less curved trajectories (Fig. 1 *B–E* and Video S1). As DNA concentration was increased, the magnitude of mean curvature of cell trajectories decreased monotonically and approached zero at DNA concentrations above 1,000 ng/μL (Fig. 2*A*); also the curvature distribution became narrower at higher DNA concentrations (Fig. 2*B*).

Similar curvature-reduction behavior was observed for *E. coli* swimming in viscoelastic fluids consisting of the polymers methyl cellulose and polyvinylpyrrolidone K90, although curvature reduction in the latter case was to a lesser extent (*SI Appendix*, Fig. S2 and Videos S2 and S3). In addition, the swimming speed of bacteria in DNA and methyl cellulose solutions increased by up to half at optimal concentrations (Fig. 2*A* and *SI Appendix*, Fig. S2*B*), in agreement with previous studies done in bulk fluids with viscoelastic and shear-thinning properties (9, 14–17). We note that straightening of swimming trajectory was reported for bacteria swimming in the bulk of polymer solutions (15); the phenomenon refers to the reduction of high-frequency positional fluctuations on the order of ~1 μm at the wobbling time scale (~<0.1 s) compared with trajectories of cells in Newtonian fluids. Here, in our study, the curvature measurement was performed for cell trajectories lasting for >~20 μm in length (or >1 s in duration), during which any effect due to the wobbling-induced high frequency positional fluctuations is smoothed out.

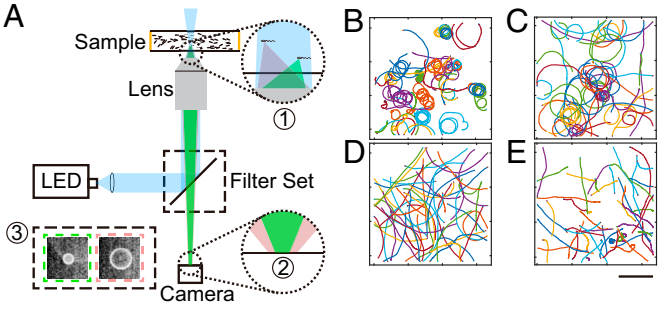

Fig. 1. Diagram of 3D defocused fluorescence microscopy and representative bacterial trajectories in DNA solutions. (*A*) Excitation light (blue) from an LED light source passes through an FITC filter set and is focused near the bottom of the sample chamber filled with a bacterial suspension and sealed by Vaseline (yellow). Fluorescence emission from bacterial cells at different height above the bottom surface of the chamber (*Inset 1*) reaches different areas of the camera sensor (*Inset 2*), and the signals are output by the camera as defocused rings of different radius (*Inset 3*). (*B–E*) 2D projection of 3D trajectories of *E. coli* (smooth-swimming mutant; YW268) tracked near glass surface immersed in fluids with (*B*) 0 ng/μL, (*C*) 500 ng/μL, (*D*) 1,000 ng/μL, and (*E*) 3,000 ng/μL DNA. Each trajectory starts with a dot. (Scale bars in *B–E*: 200 μm.)

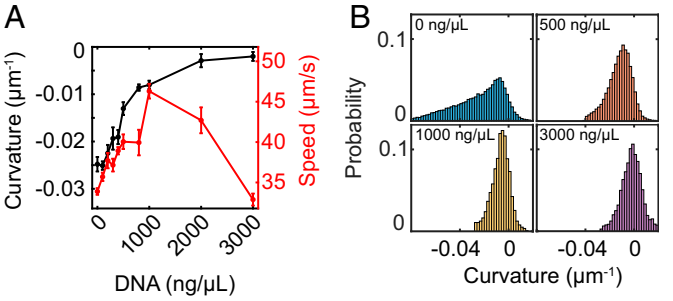

Fig. 2. Curvature analysis of cells near solid surface immersed in DNA solutions. (*A*) Signed curvature (black) and swimming speed (red) of cells at different DNA concentrations (from 0 ng/μL to 3,000 ng/μL). The curvature was computed based on 2D-projected trajectories of cells. Negative (or positive) sign of curvature indicates clockwise (or counterclockwise) circular motion. Error bars indicate SEM ($n = 10$ replicates). Lines serve as guides to the eye. (*B*) Curvature distribution of the trajectories at different DNA concentrations. Data in this figure was from a representative experiment; five biological replicates were performed and they showed the same behavior despite cell speed variation between samples.

Viscoelasticity of Polymeric Fluids Reduces Near-Surface Accumulation of Bacteria. First discovered in spermatozoa (42), near-surface accumulation is a well-studied phenomenon of microswimmers and robustly observed in flagellated bacteria (28, 29, 43). With 3D single-cell tracking, we were able to examine this phenomenon for bacteria swimming in viscoelastic polymer solutions by measuring the density distribution of bacteria at different heights from a solid surface. We found that as the DNA concentration was increased, the steady-state cell density distribution showed reduced near-surface accumulation (Fig. 3*A*). Among cells found within 20 μm from the surface, 96.0 ± 0.3% (mean ± SD) appeared in the range of ~1–5 μm in Newtonian fluids, whereas the percentage dropped to 83.0 ± 0.4%, 76.2 ± 0.8%, and 48.0 ± 5.0% in fluids with DNA concentration 500, 1,000, and 3,000 ng/μL, respectively (Fig. 3*B*). We also assessed the tendency for cells to escape from the surface at different heights using a quantity called surface-escaping rate, which is defined as the number of events of moving away from the surface per cell per unit time (*Materials and Methods*). As shown in Fig. 3*C*, the surface-escaping rate at heights below 10 μm increased with DNA concentrations, and the rates leveled off at similar constant values at heights beyond 10 μm in all cases.

Again, similar results were obtained for *E. coli* swimming in solutions of methyl cellulose and polyvinylpyrrolidone K90 (*SI Appendix*, Fig. S3 *A–F*). By contrast, these behaviors are not observed for cells in Newtonian fluids (Fig. 3 *D–F* and *SI Appendix*, Fig. S3 *G–I*). Taken together, the results presented in Fig. 3 showed that cells in viscoelastic solutions are more likely to escape from the surface than cells in Newtonian fluids. In addition, we found that the cell density distributions near the top surface of the fluid chamber were similar to those measured near the bottom surface. Therefore, sedimentation due to

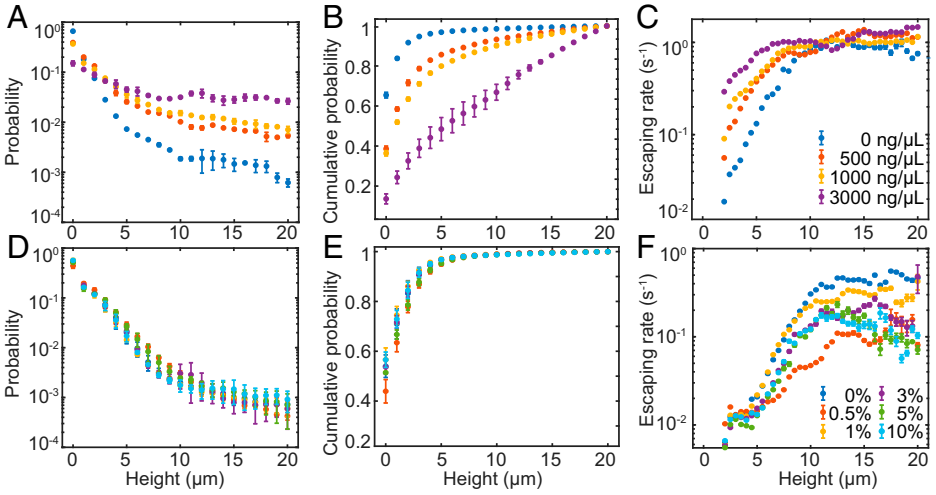

Fig. 3. Cell density distribution near a solid surface in viscoelastic and Newtonian fluids. DNA (*A–C*) and polyethylene glycol (PEG; *D–F*) solutions were used as representative viscoelastic and Newtonian fluids, respectively. (*A* and *D*) Cell density distribution as a function of cell distance to surface (or height above the surface). (*B* and *E*) Cumulative distribution of cell density as a function of cell distance to surface. (*C* and *F*) Cell escaping rate (*Materials and Methods*) as a function of cell distance to surface. Colors correspond to different DNA (blue, 0 ng/μL; red, 500 ng/μL; yellow, 1,000 ng/μL; and purple, 3,000 ng/μL) or PEG solutions (blue, 0%; red, 0.5%; yellow, 1%; purple, 3%; green, 5%; and cyan, 10%). Error bars indicate SD (for *A*, *B*, *D*, and *E*, $n = 3$ technical replicates; for *C* and *F*, $n > 36$ technical replicates). Data in this figure were from representative experiments; five and two biological replicates were performed for (*A–C*) and (*D–F*), respectively, and they showed similar behavior despite variation in cell speed and density between samples.

gravity has negligible effect on the near-surface cell density profiles during our measurement.

Hydrodynamic Modeling Reveals a Viscoelastic Lift Force Acting on Bacterial Flagellum. A number of physical processes have been shown to play important roles in the near-wall accumulation and circular swimming in Newtonian fluids, including both short-range and long-range hydrodynamic interactions, direct collisions, and Brownian motion (24, 28, 29, 31, 32, 43, 44). Far-field hydrodynamic attraction, in particular, has been shown to predict cell accumulation within several cell body lengths from solid surfaces (28), in agreement with our results measured in Newtonian fluids. Since our experimental findings show reduced near-surface accumulation in viscoelastic polymeric liquids, we hypothesize that the reduction arises from a decrease of this far-field hydrodynamic attractive effect. To test this hypothesis, we sought to compute the hydrodynamic forces acting on a swimming bacterium near a solid surface (*Materials and Methods* and *SI Appendix*, Text). As we show below, the predictions of the resulting model agree with our data, giving support to our hypothesis.

An *E. coli* cell typically consists of short body (~2 μm in length) and a long flagellar bundle [~5–10 μm in length (45)]. As the body rotates at much smaller frequency than the flagellar bundle and thus contributes less to the hydrodynamic interaction between the cell and the surface, we neglected the cell body in our non-Newtonian analysis (the *SI Appendix*, Text provides further justification). We considered a cylinder of radius R, modeling the "effective" flagellar bundle, the axis of which is located at distance d and parallel to a plane wall. Modeling the flow around a flagellar filament with a rotating cylinder can be justified by numerical simulations showing that the translational flow component due to the chirality of a rotating helical filament is about two orders of magnitude weaker than the azimuthal flow component (46), and that the averaged azimuthal component is well approximated with a rotating cylinder (47) (*SI Appendix*, Text includes more discussion). The cylinder is rotating in a counter clockwise fashion (viewed from behind the cell) with constant angular velocity ω as shown in Fig. 4*A*. In the Newtonian case, the hydrodynamic force acting on the cylinder in the direction perpendicular to the surface (i.e., the lift force) is zero by symmetry of the Stokes equations, relevant here given the very low Reynolds numbers of swimming bacteria (48). In the non-Newtonian case, nonlinear polymeric stresses are generated in the fluid, which may lead to nonzero lift, and we aimed to estimate the magnitude of that lift. We first performed this calculation analytically in the case of small deviations from a Newtonian fluid, specifically using the second-order viscoelastic fluid model (33). Exploiting the Plane Flow theorem of Tanner and Pipkin (33), we found a lift force F_{lift} acting on the rotating cylinder (per unit length) and away from the surface in the following analytical form (*SI Appendix*, Text):

$$F_{lift} = 2\pi \mathrm{De} R\omega\eta_0 \left(\left(\frac{d}{R}\right)^2 - 1 \right)^{-\frac{3}{2}}. \qquad [1]$$

Here, R is the helical radius of a flagellum, η_0 is the zero-shear viscosity of the polymer solution and De is the dimensionless Deborah number, product of the rotation frequency and the relaxation time of the polymeric fluid (*SI Appendix*, Text). This lift force is seen to be smaller at higher distance from the surface or for smaller cylinder radius (Fig. 4*B*); since it always acts away from the surface, it always weakens the hydrodynamic interactions and is consistent with the experimental observations. Numerical simulations with Oldroyd-B and Giesekus fluids (33) for small De (=0.05) also yielded a lift force in good agreement with the analytical solution (Fig. 4*B* and *SI Appendix*, Text). Nonetheless, the second-order fluid approximation is valid for small deviations from the Newtonian case, i.e., for $\mathrm{De} \ll 1$ only. In our experiments, the De numbers of the flagellum far exceed 1 given the high shear rate ($\dot{\gamma} \approx 10^4$ Hz) and the Zimm time scale (relaxation time of a single polymer) being ~2–6 ms (*SI Appendix*). At high De, polymer coils in a semidilute solution are stretched in the flow and viscosity would decrease. As such, shear-thinning viscosity should be taken into account in order to compute the lift force

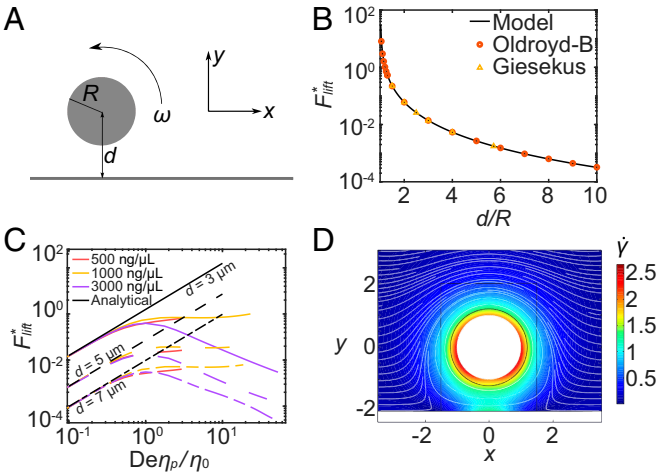

Fig. 4. Viscoelastic lift force acting on a modeled bacterial flagellum. (*A*) Sketch of the geometry for 2D model of bacterial flagellum rotating near a solid surface. (*B*) Rescaled lift force $F_{lift}/R\omega\eta_0$ as a function of d/R with fixed De = 0.05. Open circles denote numerical solution using Oldroyd-B fluid and hollow triangles denote numerical solution for Giesekus fluid in COMSOL Multiphysics. (*C*) Lift force estimated from Giesekus fluid simulations for rheology reported in *SI Appendix*, Table S1 as a function of De for $d = 3$ μm (solid line), $d = 5$ μm (dashed), and $d = 7$ μm (dash-dotted) (*SI Appendix*, Text). The corresponding force for second-order fluid is shown with black lines. (*D*) Shear magnitude distribution defined as $\dot{\gamma} = \sqrt{(\dot{\gamma} : \dot{\gamma})/2}$ (*SI Appendix*, Text) and streamlines around the modeled flagellum in Newtonian (and second order) fluid for $d/R = 2$. Color map indicates magnitude of the dimensionless shear rate.

at high De. We performed numerical simulations for a model shear-thinning viscoelastic fluid (Giesekus fluid (33)) using parameters in line with those obtained in experiments (*SI Appendix*, Table S1 and Fig. S4). As shown in Fig. 4*C*, the linear dependence of the force on De predicted in Eq. 1 for the second-order fluid breaks down around De ≈ 1, where the lift force starts to plateau or decay, in part due to shear-thinning. In our experiments, more concentrated DNA solutions have higher De (*SI Appendix*, Table S1).

The viscoelastic lift force we uncovered here arises from the following physical mechanism. Strain in the flow leads to polymer stretching; the polymer molecules resist this imposed stretching away from their equilibrium configuration and as a result pull back on the flow in response. This leads to an additional tension (i.e., a negative pressure) generated along flow streamlines (49). In the context of non-Newtonian fluid mechanics, this is known as a normal stress difference, and it scales quadratically with the rate of deformation (since reversing the direction of the flow leaves the tension unchanged). These normal stress differences generated along curved streamlines around a rotating flagellum will result in forces perpendicular to the wall: the elastic tension on the side of the flagellum close to the wall is higher because of the higher extension rate there (Fig. 4*D*). Consequently, a net perpendicular force (i.e., the lift force) pushes the flagellum away from the wall. This mechanism is similar to that responsible for the clustering of particles sedimenting in viscoelastic fluids (50). This lift is expected to be a generic result for rotating bodies near a solid surface immersed in viscoelastic fluids. It is related to past work revealing lift exerted on a sphere very close to a plane wall in a shear flow (51) and is analogous to lift induced by a polymer-grafted cylinder translating parallel to an elastic wall in a Newtonian fluid (52).

Lift Force Combined with Hydrodynamic Attraction Reproduces Near-Surface Cell Density Profiles. Next, we sought to estimate near-surface bacterial density profiles using the lift force found above. To do so, we first need to find the drift velocity u perpendicular to the surface (along y-axis in Fig. 4*A*), which is the sum of velocities resulting from the lift force (u_{lift}) and from hydrodynamic attraction by the surface (u_a). The vertical lift velocity u_{lift} is estimated by balancing the lift by both the drag on the head $\eta_0 C_b$ (taken to be that on a translating sphere) and the drag on the filament $\eta_N C_f$ (estimated as that of a translating helix in the y direction, see *SI Appendix*, Text) leading to

$$u_{lift} = \frac{F_{lift}\, L}{C_b\eta_0 + C_f\eta_N}. \quad [2]$$

Meanwhile, for an *E. coli* cell swimming parallel to the surface, the attractive far-field (Newtonian) velocity in y-direction has been derived in a three-dimensional theory as being $u_a = -\frac{3p}{64\pi\eta_0}\frac{1}{y^2}$, where $p = F_{prop}l$ is the force dipole of the cell with F_{prop} the propulsive force of the flagellum, $l \approx 10\ \mu$m the cell length (including cell body and flagellar bundle) (28). The propulsive force of *E. coli* can be expressed as $F_{prop} = \hat{b}\omega\eta_N$, with $\hat{b}$ being a geometrical constant and η_N the viscosity at the filament level. As the flagellum operates approximately at constant torque, F_{prop} is the same for all DNA solutions used in our experiment, and is estimated to be $F_{prop} \approx 0.3$ pN (*SI Appendix*). Note that $u_a \sim 1/\eta_0$ will decrease in magnitude for higher DNA concentrations. Summing up both velocities we predicted a total drift velocity given by $u = u_{lift} + \xi u_a$ as plotted in Fig. 5*A*, where ξ is an order-one dimensionless factor allowing to combine in a single formula the far-field three-dimensional attraction (u_a) with the near-field two-dimensional lift (u_{lift}) in the "intermediate" regions where both formulae are valid (28).

The total drift velocity obtained above allows us to estimate the near-surface cell density profile using a previously proposed advection-diffusion model (28). Denoting the cell density as $n(y)$, and balancing the advective and diffusive transport (with $D_\perp$ being the diffusion coefficient of the cells perpendicular to the surface), we have:

$$\frac{\partial(nu)}{\partial y} = D_\perp \frac{\partial^2 n}{\partial y^2}. \quad [3]$$

Integrating this expression once and using that $\partial n/\partial y \to 0$ as $y \to \infty$, we simplified Eq. 3 to $nu = D_\perp \partial n/\partial y$. This equation is solved numerically with boundary condition $n(y = 10\ \mu\text{m}) = n_0$ (*SI Appendix*, Text) to yield the cell density profiles in Fig. 5*B*, which agree well with those obtained in experiments. We have also solved for the concentrations in PVP and MC fluids (*SI Appendix*, Fig. S5 and Text for the analytical solution). In that

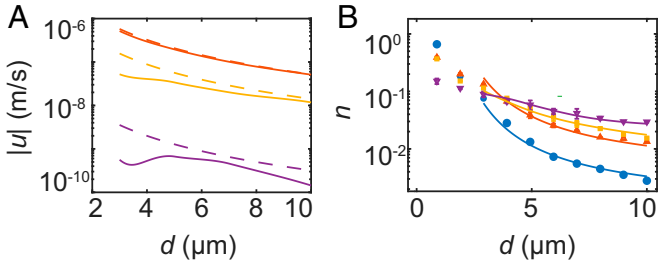

Fig. 5. Drift speed and cell density profiles near a solid surface. (*A*) Hydrodynamic attractive velocity (ξu_a; dashed) and total drift velocity ($u_{lift} + \xi u_a$; solid) as functions of distance to the wall for 500 ng/μL (red), 1,000 ng/μL (yellow), and 3,000 ng/μL (purple) DNA solutions. (*B*) Cell density profiles as a function of distance to the wall for different DNA solutions (blue, 0 ng/μL; red, 500 ng/μL; yellow, 1,000 ng/μL; and purple, 3,000 ng/μL). Scattered points are experimental data; solid lines are computed from the model using the dipole $p = F_{prop}l$ with $\xi = 0.56$ (for the attraction) and varying the values of n_0 for each curve. See also *SI Appendix*, Text.

case, the agreement between the experiments and our model is not as good as with the DNA solutions. We speculate that this is due to the De numbers being several orders of magnitudes smaller than that for highly elastic DNA solutions, resulting in much smaller lift force and therefore a higher sensitivity of our theoretical predictions to other approximations made in our model. Note that reduced near-surface accumulation was previously predicted for bacteria swimming in shear flows of weakly viscoelastic fluids but the analysis resorted to Newtonian hydrodynamic interactions (18).

Finally, to address the reduction in curvature of the trajectories, we may use the model developed in Lauga et al. (24) for Newtonian fluids to predict the size of the radius of curvature using the distribution of surface distances reported experimentally in Fig. 3*A*. We found that the increased mean distance to the wall of bacteria in polymeric liquids is only partially responsible for the reduction of curvature (*SI Appendix*, Fig. S6, Table S2 and Text). Therefore, further research is necessary to determine the impact of non-Newtonian mechanisms, such as elastic forces acting parallel to the plane surface, elastic torques perpendicular to the surface and shear-thinning at the filament level.

Discussion

To summarize, we found that viscoelasticity of macromolecular polymers induces a lift force that weakens hydrodynamic interaction between microswimmers and solid surfaces. Consequently, cells display less near-surface accumulation and swim in less curved trajectories. The same swimming behavior is also seen in flagellated bacteria with wild-type run-and-tumble motion (*SI Appendix*, Fig. S7). These previously unrecognized swimming behaviors of flagellated bacteria in viscoelastic fluids are expected to have profound impact on microbial behavior in polymer-rich environments. For instance, bacterial cells dispersing from aged biofilms have to swim through the viscoelastic matrix consisting of extracellular DNA and large-molecular weight polysaccharides (1); commensal bacteria migrating in the digestive tract of animals frequently encounter mucus and food-derived macromolecular polymers (53); and pathogens invading cells and tissues explore the interstitial space filled with body fluids rich in biopolymers such as collagens and glycosaminoglycans (54, 55). During these processes, swimming in less curved trajectories will increase the directional persistence time, and reduced near-surface accumulation will decrease the likelihood of surface trapping; both effects will enhance the efficiency of bacterial transport and surface exploration. On the other hand, due to reduced near-surface accumulation, the frequency of bacteria-surface contact (or reversible surface attachment) would be lower, and thus the dynamics of biofilm initiation (56) in polymeric environments should be re-evaluated. Notably, the extracellular DNA concentrations in the biofilm matrix of several bacterial species (including *E. coli*) are on the order of ∼1,000 ng/μL (57), and the concentration of environmental DNA in sputum from lungs is between 2000–20,000 ng/μL (58); the DNA concentrations we used in this study (hundreds to thousands ng/μL) are of comparable orders of magnitude, thus our results are physiologically relevant.

Our findings are also pertinent to the locomotion of synthetic helical microswimmers (36) in polymeric fluids. Artificial helical microswimmers driven by rotating magnetic field are promising tools for biomedical applications such as microsurgery and targeted drug delivery in the human body (59). It is often desirable to drive the locomotion of artificial microswimmers near tissue surfaces with complex topography or through narrow ducts (60). Since viscoelastic polymers are pervasive in physiological environments, our results will provide insight to these transport processes of artificial helical microswimmers. In addition, our analysis showed that hydrodynamic interactions between artificial helical microswimmers and rigid surfaces in viscoelastic fluids can be tuned by helical radius (Fig. 4*B*). This mechanism could be employed to enrich the locomotor repertoire of smart artificial microswimmers (61), such as those with shape-changing capability (62), allowing them to navigate through complex geometries and locate the pathological sites more efficiently.

Materials and Methods

Bacterial Strains and Materials. The following bacterial strains were used: *E. coli* HCB1 (wild-type) and HCB1736 (a derivative of *E. coli* AW405 with *cheY* deletion and smooth-swimming behavior), gifts from Howard Berg, Harvard University, Cambridge, MA; *E. coli* YW191 [*E. coli* HCB1 transformed with pAM06-tet plasmid carrying kanamycin resistance and expressing green fluorescent protein (GFP) constitutively; the pAM06-tet plasmid was a gift from Arnab Mukherjee and Charles M. Schroeder, University of Illinois at Urbana-Champaign (63)]; and *E. coli* YW268 (*E. coli* HCB1736 transformed with pAM06-tet plasmid). Plasmids were transformed via electroporation. The following polymers were used: salmon testes DNA (abbreviated as DNA; ∼2,000 base pair, molecular weight M_w ∼1.3 MDa, Sigma-Aldrich, cat. no. D1626), polyethylene glycol (PEG, M_w ∼8 kDa, Sigma-Aldrich, cat. no. 89510), polyvinylpyrrolidone K90 (PVP, M_W ∼0.36 MDa, Sigma-Aldrich, cat. no. 81440), Ficoll 400 (M_W ∼0.4 MDa, Sigma-Aldrich, cat. no. F9378), and hydroxypropyl methyl cellulose (MC, M_W ∼86 kDa, Sigma-Aldrich, cat. no. H7509).

Bacterial Growth and Sample Preparation. Single-colony isolates of *E. coli* (picked from streaked plates stored at 4 °C) were grown overnight (∼12 h) with shaking in LB medium (1% Bacto tryptone, 0.5% yeast extract, 0.5% NaCl) at 30 °C to stationary phase. 30 μL overnight culture was then diluted 10^{-2} in TB medium (1% Bacto tryptone and 0.5% NaCl) and further grown with shaking for 5 h, yielding a bacterial culture with a density of ∼10^8 cells/mL (determined by OD_{600} measurement) and a typical cell length of ∼1–2 μm (∼0.8 μm in diameter). The obtained culture was diluted 10^{-3}, mixed with polymer solutions (dissolved in TB medium) and injected into a glass chamber sealed with Vaseline for imaging. The size of the glass chamber was ∼2 cm × 1 cm × 1 mm (length × width × height). The final cell density in the chamber was sufficiently low to ignore cell–cell interactions.

Imaging and Single-Cell Tracking. We used 3D defocused fluorescence microscopy to perform 3D tracking of single-cell trajectories (40). Imaging was performed on a Nikon TI-E microscope through a 20× objective (Nikon CFI Plan Fluor DLL 20×, numerical aperture 0.50, working distance 2.1 mm). Fluorescence imaging of cells labeled with GFP was performed in epifluorescence using an FITC filter set (excitation 482/35 nm, emission 536/40 nm, dichroic: 506 nm; FITC-3540C-000; Semrock Inc.), with the excitation light provided by a mercury precentered fiber illuminator (Nikon Intensilight). Recordings were made with a scientific complementary metal-oxide-semiconductor (sCMOS) camera (Andor Zyla 4.2 PLUS USB 3.0 or Andor Neo 5.5; Andor Technology) (35 ms exposure time, 20 fps). The schematic diagram of the imaging setup is shown in Fig. 1*A*. The imaging was performed at room temperature (∼22 °C). 3D trajectories of cells were obtained based on the recorded videos using a custom-written tracking program in MATLAB 2018a (The MathWorks). The tracking program consists of the following two components, a tracking library and a single-cell tracking algorithm.

(a) Tracking library. A cell in the focal plane appears as a spot or a short rod in fluorescence images. As the cell moved away from the focal plane, its image will defocus and appear as a circular defocused ring (Fig. 1*A*). The radius of the defocused ring is positively correlated with the distance between the focal plane and the cell's centroid (40). A tracking library is a database that allows us to quantify the relation between the radius of defocused rings and the height above the focal plane. To establish the tracking library, we first took an image stack of fluorescent cells attached to the bottom chamber surface at various distances from the focal plane while moving the vertical axis of microscope stage.

To find the radius of defocused rings, each image was processed with a Gaussian blur to reduce the background noise and then converted into a binary (black and white) image by thresholding at an appropriate pixel intensity. We used circular Hough transform (a built-in function of MATLAB) to fit circles in the binarized image. Specifically, a defocused ring is assumed to be a circle in x-y plane described by $(x-a)^2+(y-b)^2=r^2$, where (a, b) is the center and r is the radius. The purpose is to find an optimal parameter set (a, b, r) that best fits the defocused ring to a circle. The position of pixel i of the defocused ring in the binarized image is (x_i, y_i), and for each pixel this pair of x-y coordinates defines a cone-like shape in 3D parameter space of (a, b, r) in the form of $(a-x_i)^2+(b-y_i)^2=r^2$. The cones defined by all the pixels belonging to a defocused ring will intersect with each other in the 3D parameter space of (a, b, r). Then the point (a_0, b_0, r_0) in parameter space belonging to the most cones is defined as the optimal parameter set and selected as the parameters to define the optimal circle fit of the defocused ring. Having obtained the radius of defocused rings at different distances to the focal plane for an ensemble of typical cells ($n=5$), we found that the radius of defocused rings (r) and the distance to focal plane (h) followed a linear relation $r=Ah+b$, with $A=1.19$ μm/pixel.

(b) Single-cell tracking algorithm. We set the focal plane as close to the bottom surface of the glass chamber as possible and took time-lapse videos of cells swimming near the bottom surface as mentioned above. Images in a video were first processed by similar denoise method and Circular Hough Transform mentioned above to find circles in the images. 3D positions of cells in the images were obtained from the centers of defocused rings (yielding the coordinates in horizontal plane) and from the radius of defocused rings (yielding vertical position coordinates relative to the focal plane). Then single-cell trajectories were tracked using an algorithm described in a previous study (64). Briefly, each image was segmented into Thiessen (or Voronoi) polygons and each polygon only contained the position of one bacterium. For any two consecutive image frames (say, frame n and frame n+1), if there was one and only one bacterial position in the same polygon for both frame n and n+1, the two cells were taken as the same one and thus its trajectory from frame n to frame (n+1) was obtained; iterate this step for all frames in the time-lapse video to obtain the complete trajectory of all cells. The distance between the focal plane and the bottom surface of the glass chamber was computed as the mean of the lowest vertical position of all trajectories; this value allowed us to obtain the height of cells from the bottom surface. To determine the spatial resolution of tracking, we tracked stationary cells attached to a glass surface and found that the measurement error (SD) of position coordinates was 0.40 μm and 0.86 μm for horizontal and vertical position coordinates, respectively.

Rheological Measurement. Shear viscosity of polymer solutions (*SI Appendix*, Fig. S4*B*) were measured by bulk rheometry with a rheometer (Anton Paar Physica MCR 301) at room temperature (~22 °C). The plate used for shear viscosity measurement was CP50-1 (diameter 49.972 mm, angle 0.990°, and 99 μm gap; Anton Paar, part no. 79040 serial 20173). During measurement, a ramp of shear rate (from 0.1 s^{-1} to 10^4 s^{-1}) was applied. The relaxation time and zero shear viscosity for Giesekus fluid calculations were estimated based on the dynamic moduli of polymer solutions measured by microrheology (65–67); note that the rheometer for bulk rheometry does not have sufficient resolution to probe the low-frequency dynamic moduli of our polymer solutions or to work at low shear rate. Microrheology measurement was performed at room temperature (~22 °C) following a protocol described in a previous study (39). Polymer solutions dissolved in buffer (TB medium) were supplemented with 1.0 μm diameter microspheres (Polysciences, cat. no. 19404) and sealed by Vaseline in a glass chamber with depth ~1,000 μm. The glass chamber was held stationary for several hours before microrheology measurement in order to minimize advection. Mean square displacement (MSD) of microspheres were measured by tracking the microspheres in polymer solutions in the glass chamber based on phase contrast images taken with a 60× air objective (Nikon Plan Apo λ, numerical aperture 0.95, working distance 0.20–0.11 mm) and a 1.5× relay lens equipped on the microscope. The focal plane was chosen to be near the middle of the glass chamber and at least 50 μm away from the solid walls. For each sample, the motion of >3 different microspheres was recorded with the sCMOS camera (Andor Zyla 4.2) at 25 fps each for a duration of >~30 min. The number density of microspheres was sufficiently low, such that there was typically only one microsphere in the field of view during recording. The trajectories of microspheres were tracked by a custom-written program in MATLAB. Dynamic moduli of polymer solutions was computed based on the MSD of microspheres and a frequency-dependent Stokes–Einstein equation (65) using a MATLAB algorithm (Kilfoil laboratory at the University of Massachusetts, Amherst). The relaxation time of polymer solutions (τ) was calculated from the lowest crossover frequency (denoted as ω_c) between storage modulus (G′) and loss modulus (G″) as $\tau=1/\omega_c$; for polymer solutions without lowest crossover frequency (e.g., 500 ng/μL DNA solutions), τ was computed by $\tau=12(\eta-\eta_s)/(\pi^2\rho k_BT)$ (68), where η is zero-shear viscosity of the polymer solutions computed by fitting $G''=\eta\omega$ in low frequency regime (0.05^{-1} s^{-1}), η_s is the shear viscosity of the buffer (TB medium), ρ is number density of polymer molecules in unit m^{-3}, and k_B is Boltzmann constant, and T is room temperature (~22 °C).

Data Analysis. When analyzing curvature and swimming speed of cells near a solid surface, only those trajectories lasting longer than 1 s and within 5 μm from the surface were selected. When analyzing density distribution and motion of cells in the bulk of fluids, all trajectories lasting longer than 1 s were used. For each polymer concentration, at least 1,000 trajectories were sampled (except 831 trajectories for 0.6% methyl cellulose and 708 trajectories for the buffer free of additive polymers). To compute curvature and speed of cells near a solid surface, the selected trajectories were segmented into 1-s traces. Each segmented trace (denoted as S_i, $i=1,2,\ldots N$, with N being the total number of segmented traces) was fitted to a circle with radius r_i on the solid surface plane. The signed curvature of S_i was then $\pm 1/r_i$, with the negative (or positive) sign denoting clockwise (or counterclockwise) circular motion (viewed from liquid to the solid surface). The curvature of a trajectory is taken as the mean of S_i. Cells in the bulk of DNA solutions are not expected to swim in circles; but to verify this fact, the curvature of their trajectories were analyzed in the same manner (*SI Appendix*, Fig. S8). To calculate bacterial density distribution near the solid surface, the normalized cell density at a specific height z_0 from the surface was defined as the number of trajectory points falling into the space $(z_0-0.5\ \mu m)\le z\le(z_0+0.5\ \mu m)$ divided by all trajectory points in the space $0\le z\le 20\ \mu m$ during the entire tracking period. To calculate surface-escaping rate of bacteria, we divided the space ranging from 2 μm to 20 μm above the solid surface into slices confined by parallel planes with a constant separation of 0.5 μm, and for each plane, the average absolute vertical speed $|V_\perp|$ was calculated for all trajectories below the plane (we noted that $|V_\perp|$ increased with height above the surface). For a specific plane σ at height $z=z_0$, we considered surface-escaping events within a duration of $\Delta t_\sigma=H/|V_\perp|$ and contributed by cells within $(z_0-H)\le z\le z_0$, where H was set as 2 μm to avoid counting multiple surface-escaping events by the same cell during Δt_σ. For a time-lapse video of duration T, the surface-escaping rate at plane σ was computed as follows in $m=T/\Delta t_\sigma$ time windows, with the i-th time window denoted as $\Delta t_{\sigma,i}$, $i=1, 2, \ldots, m$ (1): the cell number within $(z_0-H)\le z\le z_0$ for each image frame in time window $\Delta t_{\sigma,i}$ was first computed and the average cell number per frame was taken as $n_{\sigma,i}$ (2); denoting the z axis measurement error (0.86 μm; see the "Imaging and Single-Cell Tracking" section above) as ξ, a surface-escaping event at plane σ was defined as a cell first passing the $z=z_0-\xi$ plane and then passing the $z=z_0+\xi$ plane within the time window $\Delta t_{\sigma,i}$, and we calculated the number of all such surface-passing events as $S_{\sigma,i}$ for the plane σ based on cell trajectories within $\Delta t_{\sigma,i}$ (3); finally the surface-escaping rate for the plane σ during the tracking period was computed as $r_\sigma=\frac{1}{m}\sum_{i=1}^{m}\frac{S_{\sigma,i}}{n_{\sigma,i}\cdot\Delta t_\sigma}=\frac{1}{T}\sum_{i=1}^{m}\frac{S_{\sigma,i}}{n_{\sigma,i}}$.

There were some extreme and unrealistic values of curvature and cell speed (e.g., swimming speed >80 μm/s in buffer) due to the resolution of spatial and temporal measurement. We denoted a value as an outlier if it was more than three scaled median absolute deviations (MAD) (69) greater than the median. For N measurements of quantity A, the MAD is defined as $MAD=median(|A_i-median(A)|)$ where $i=1, 2, \ldots, N$. These outliers were not used when plotting the distributions.

Hydrodynamic Model. A detailed hydrodynamic model is described in the *SI Appendix*, Text. We start with second-order fluid approximation, which is valid at small De numbers. It allows us to calculate the lift force in Eq. **1** analytically. We then estimate De numbers for rotating filament and find that they are much

larger than 1, requiring full numerical simulations as described. Finally, we estimate the lift velocity and combine it with hydrodynamic attraction and estimate the concentration of the cells away from the wall.

Data, Materials, and Software Availability. All study data are included in the article and/or *SI Appendix*.

ACKNOWLEDGMENTS. Y.W. and E.L. would like to acknowledge their debt to the late Howard C. Berg, an inspiring mentor and collaborator who sadly passed away in December 2021. We thank Arnab Mukherjee and Charles M. Schroeder (UIUC) for their kind gift of plasmid. Yuhao Wang (CUHK) helped with 3D defocused microscopy. This work was supported by the National Natural Science Foundation of China (31971182, to Y.W.), the Research Grants Council of Hong Kong SAR (14306820, RFS2021-4S04, and CUHK Direct Grants to Y.W.), and the European Research Council under the European Union's Horizon 2020 Research and Innovation Programme (682754 to E.L.).

Author affiliations: [a]Department of Physics and Shenzhen Research Institute, The Chinese University of Hong Kong, Shatin, NT, Hong Kong, People's Republic of China; and [b]Department of Applied Mathematics and Theoretical Physics, University of Cambridge, Cambridge, CB3 0WA United Kingdom

Author contributions: D.C. designed the study, performed experiments, analyzed and interpreted the data. M.D. and E.L. developed the hydrodynamic model. S.L. discovered the phenomena, designed the study and performed initial experiments. Y.W. designed the study, analyzed and interpreted the data. E.L. and Y.W. supervised the study. Y.W. wrote the paper with input from other authors.

1. H.-C. Flemming, J. Wingender, The biofilm matrix. *Nat. Rev. Microbiol.* **8**, 623–633 (2010).
2. B. O. Schroeder, Fight them or feed them: How the intestinal mucus layer manages the gut microbiota. *Gastroenterol. Rep. (Oxf.)* **7**, 3–12 (2019).
3. O. Chaudhuri, J. Cooper-White, P. A. Janmey, D. J. Mooney, V. B. Shenoy, Effects of extracellular matrix viscoelasticity on cellular behaviour. *Nature* **584**, 535–546 (2020).
4. A. Persat *et al.*, The mechanical world of bacteria. *Cell* **161**, 988–997 (2015).
5. S. B. Guttenplan, D. B. Kearns, Regulation of flagellar motility during biofilm formation. *FEMS Microbiol. Rev.* **37**, 849–871 (2013).
6. T. J. Wiles *et al.*, Swimming motility of a gut bacterial symbiont promotes resistance to intestinal expulsion and enhances inflammation. *PLoS Biol.* **18**, e3000661 (2020).
7. B. Chaban, H. V. Hughes, M. Beeby, The flagellum in bacterial pathogens: For motility and a whole lot more. *Semin. Cell Dev. Biol.* **46**, 91–103 (2015).
8. J. D. Ferry, *Viscoelastic Properties of Polymers* (John Wiley & Sons, 1980).
9. W. R. Schneider, R. N. Doetsch, Effect of viscosity on bacterial motility. *J. Bacteriol.* **117**, 696–701 (1974).
10. G. E. Kaiser, R. N. Doetsch, Letter: Enhanced translational motion of Leptospira in viscous environments. *Nature* **255**, 656–657 (1975).
11. E. P. Greenberg, E. Canale-Parola, Motility of flagellated bacteria in viscous environments. *J. Bacteriol.* **132**, 356–358 (1977).
12. H. C. Berg, L. Turner, Movement of microorganisms in viscous environments. *Nature* **278**, 349–351 (1979).
13. Y. Magariyama, S. Kudo, A mathematical explanation of an increase in bacterial swimming speed with viscosity in linear-polymer solutions. *Biophys. J.* **83**, 733–739 (2002).
14. V. A. Martinez *et al.*, Flagellated bacterial motility in polymer solutions. *Proc. Natl. Acad. Sci. U.S.A.* **111**, 17771–17776 (2014).
15. A. E. Patteson, A. Gopinath, M. Goulian, P. E. Arratia, Running and tumbling with *E. coli* in polymeric solutions. *Sci. Rep.* **5**, 15761 (2015).
16. A. Zöttl, J. M. Yeomans, Enhanced bacterial swimming speeds in macromolecular polymer solutions. *Nat. Phys.* **15**, 554–558 (2019).
17. Z. Qu, K. S. Breuer, Effects of shear-thinning viscosity and viscoelastic stresses on flagellated bacteria motility. *Phys. Rev. Fluids* **5**, 073103 (2020).
18. A. J. T. M. Mathijssen, T. N. Shendruk, J. M. Yeomans, A. Doostmohammadi, Upstream swimming in microbiological flows. *Phys. Rev. Lett.* **116**, 028104 (2016).
19. G. J. Li, A. Karimi, A. M. Ardekani, Effect of solid boundaries on swimming dynamics of microorganisms in a viscoelastic fluid. *Rheol. Acta* **53**, 911–926 (2014).
20. S. Yazdi, A. Borhan, Effect of a planar interface on time-averaged locomotion of a spherical squirmer in a viscoelastic fluid. *Phys. Fluids* **29**, 093104 (2017).
21. Z. Ouyang, J. Lin, X. Ku, Hydrodynamic properties of squirmer swimming in power-law fluid near a wall. *Rheol. Acta* **57**, 655–671 (2018).
22. H. C. Berg, L. Turner, Chemotaxis of bacteria in glass capillary arrays. *Escherichia coli*, motility, microchannel plate, and light scattering. *Biophys. J.* **58**, 919–930 (1990).
23. P. D. Frymier, R. M. Ford, H. C. Berg, P. T. Cummings, Three-dimensional tracking of motile bacteria near a solid planar surface. *Proc. Natl. Acad. Sci. U.S.A.* **92**, 6195–6199 (1995).
24. E. Lauga, W. R. DiLuzio, G. M. Whitesides, H. A. Stone, Swimming in circles: Motion of bacteria near solid boundaries. *Biophys. J.* **90**, 400–412 (2006).
25. L. Lemelle, J.-F. Palierne, E. Chatre, C. Place, Counterclockwise circular motion of bacteria swimming at the air-liquid interface. *J. Bacteriol.* **192**, 6307–6308 (2010).
26. R. Di Leonardo, D. Dell'Arciprete, L. Angelani, V. Iebba, Swimming with an image. *Phys. Rev. Lett.* **106**, 038101 (2011).
27. D. Lopez, E. Lauga, Dynamics of swimming bacteria at complex interfaces. *Phys. Fluids* **26**, 071902 (2014).
28. A. P. Berke, L. Turner, H. C. Berg, E. Lauga, Hydrodynamic attraction of swimming microorganisms by surfaces. *Phys. Rev. Lett.* **101**, 038102 (2008).
29. G. Li, J. X. Tang, Accumulation of microswimmers near a surface mediated by collision and rotational Brownian motion. *Phys. Rev. Lett.* **103**, 078101 (2009).
30. M. Molaei, M. Barry, R. Stocker, J. Sheng, Failed escape: Solid surfaces prevent tumbling of *Escherichia coli*. *Phys. Rev. Lett.* **113**, 068103 (2014).
31. S. Bianchi, F. Saglimbeni, R. Di Leonardo, Holographic imaging reveals the mechanism of wall entrapment in swimming bacteria. *Phys. Rev. X* **7**, 011010 (2017).
32. S. Bianchi, F. Saglimbeni, G. Frangipane, D. Dell'Arciprete, R. Di Leonardo, 3D dynamics of bacteria wall entrapment at a water-air interface. *Soft Matter* **15**, 3397–3406 (2019).
33. R. B. Bird, R. C. Armstrong, O. Hassager, *Dynamics of Polymeric Liquids. Vol. 1: Fluid Mechanics* (Wiley, 1987).
34. R. Rusconi, J. S. Guasto, R. Stocker, Bacterial transport suppressed by fluid shear. *Nat. Phys.* **10**, 212–217 (2014).
35. E. Perez Ipiña, S. Otte, R. Pontier-Bres, D. Czerucka, F. Peruani, Bacteria display optimal transport near surfaces. *Nat. Phys.* **15**, 610–615 (2019).
36. S. Tottori *et al.*, Magnetic helical micromachines: Fabrication, controlled swimming, and cargo transport. *Adv. Mater.* **24**, 811–816 (2012).
37. C. Bechinger *et al.*, Active particles in complex and crowded environments. *Rev. Mod. Phys.* **88**, 045006 (2016).
38. H. C. Berg, *E. coli in Motion* (Springer-Verlag, New York, 2004).
39. S. Liu, S. Shankar, M. C. Marchetti, Y. Wu, Viscoelastic control of spatiotemporal order in bacterial active matter. *Nature* **590**, 80–84 (2021).
40. M. Wu, J. W. Roberts, S. Kim, D. L. Koch, M. P. DeLisa, Collective bacterial dynamics revealed using a three-dimensional population-scale defocused particle tracking technique. *Appl. Environ. Microbiol.* **72**, 4987–4994 (2006).
41. P. P. Lele, B. G. Hosu, H. C. Berg, Dynamics of mechanosensing in the bacterial flagellar motor. *Proc. Natl. Acad. Sci. U.S.A.* **110**, 11839–11844 (2013).
42. Rothchild, Non-random distribution of bull spermatozoa in a drop of sperm suspension. *Nature* **198**, 1221–1222 (1963).
43. K.-T. Wu, Y.-T. Hsiao, W.-Y. Woon, Entrapment of pusher and puller bacteria near a solid surface. *Phys. Rev. E* **98**, 052407 (2018).
44. J. Elgeti, G. Gompper, Microswimmers near surfaces. *Eur. Phys. J. Spec. Top.* **225**, 2333–2352 (2016).
45. L. Turner, W. S. Ryu, H. C. Berg, Real-time imaging of fluorescent flagellar filaments. *J. Bacteriol.* **182**, 2793–2801 (2000).
46. S. E. Spagnolie, E. Lauga, Comparative hydrodynamics of bacterial polymorphism. *Phys. Rev. Lett.* **106**, 058103 (2011).
47. Y. Gebremichael, G. S. Ayton, G. A. Voth, Mesoscopic modeling of bacterial flagellar microhydrodynamics. *Biophys. J.* **91**, 3640–3652 (2006).
48. E. Lauga, *The Fluid Dynamics of Cell Motility* (Cambridge University Press, Cambridge, 2020).
49. G. D'Avino, P. L. Maffettone, Particle dynamics in viscoelastic liquids. *J. Non-Newt. Fluid Mech.* **215**, 80–104 (2015).
50. L. G. Leal, Particle motions in a viscous fluid. *Annu. Rev. Fluid Mech.* **12**, 435–476 (1980).
51. H. H. Hu, D. D. Joseph, Lift on a sphere near a plane wall in a second-order fluid. *J. Non-Newt. Fluid Mech.* **88**, 173–184 (1999).
52. K. Sekimoto, L. Leibler, A mechanism for shear thickening of polymer-bearing surfaces: Elasto-hydrodynamic coupling. *Europhys. Lett.* **23**, 113–117 (1993)..
53. S. S. Datta, A. Preska Steinberg, R. F. Ismagilov, Polymers in the gut compress the colonic mucus hydrogel. *Proc. Natl. Acad. Sci. U.S.A.* **113**, 7041–7046 (2016).
54. J. K. Struthers, R. P. Westran, *Clinical Bacteriology* (CRC Press, 2003), pp. 192.
55. O. Cenaj *et al.*, Evidence for continuity of interstitial spaces across tissue and organ boundaries in humans. *Commun. Biol.* **4**, 436 (2021).
56. G. A. O'Toole, G. C. Wong, Sensational biofilms: Surface sensing in bacteria. *Curr. Opin. Microbiol.* **30**, 139–146 (2016).
57. J. Wu, C. Xi, Evaluation of different methods for extracting extracellular DNA from the biofilm matrix. *Appl. Environ. Microbiol.* **75**, 5390–5395 (2009).
58. J. L. Potter, S. Spector, L. W. Matthews, J. Lemm, Studies on pulmonary secretions. 3. The nucleic acids in whole pulmonary secretions from patients with cystic fibrosis, bronchiectasis, and laryngectomy. *Am. Rev. Respir. Dis.* **99**, 909–916 (1969).
59. J. Li, B. Esteban-Fernández de Ávila, W. Gao, L. Zhang, J. Wang, Micro/nanorobots for biomedicine: Delivery, surgery, sensing, and detoxification. *Sci. Robot.* **2**, eaam6431 (2017).
60. B. Wang *et al.*, Endoscopy-assisted magnetic navigation of biohybrid soft microrobots with rapid endoluminal delivery and imaging. *Sci. Robot.* **6**, eabd2813 (2021).
61. A. C. H. Tsang, E. Demir, Y. Ding, O. S. Pak, Roads to smart artificial microswimmers. *Advanced Intelligent Systems* **2**, 1900137 (2020).
62. H.-W. Huang *et al.*, Adaptive locomotion of artificial microswimmers. *Sci. Adv.* **5**, eaau1532.
63. A. Mukherjee, J. Walker, K. B. Weyant, C. M. Schroeder, Characterization of flavin-based fluorescent proteins: An emerging class of fluorescent reporters. *PLoS One* **8**, e64753 (2013).
64. W. Zuo, Y. Wu, Dynamic motility selection drives population segregation in a bacterial swarm. *Proc. Natl. Acad. Sci. U.S.A.* **117**, 4693–4700 (2020).
65. T. G. Mason, D. A. Weitz, Optical measurements of frequency-dependent linear viscoelastic moduli of complex fluids. *Phys. Rev. Lett.* **74**, 1250–1253 (1995).
66. T. G. Mason, K. Ganesan, J. H. van Zanten, D. Wirtz, S. C. Kuo, Particle tracking microrheology of complex fluids. *Phys. Rev. Lett.* **79**, 3282–3285 (1997).
67. X. Zhu, B. Kundukad, J. R. van der Maarel, Viscoelasticity of entangled λ-phage DNA solutions. *J. Chem. Phys.* **129**, 185103 (2008).
68. B. Kundukad, J. R. C. van der Maarel, Control of the flow properties of DNA by topoisomerase II and its targeting inhibitor. *Biophys. J.* **99**, 1906–1915 (2010).
69. C. Leys, C. Ley, O. Klein, P. Bernard, L. Licata, Detecting outliers: Do not use standard deviation around the mean, use absolute deviation around the median. *J. Exp. Soc. Psychol.* **49**, 764–766 (2013).